Understanding and tuning sliding friction

Liefferink, R.W.

Publication date
2021

CHAPTER 6

Sliding friction of geometrically controlled surfaces

It is our everyday experience that two smooth surfaces slide more easily over each other than two rough ones. Counterintuitively, roughness at the nanoscale can lead to superlubricity, where the roughness actually decreases friction to extremely low values. Structural superlubricity is a property of periodic surfaces, and is attributed to the commensurability of the two surfaces sliding past each other. Here we investigate surfaces with macroscopic periodic roughness sliding over each other, allowing to directly vary the (in)commensurability of the roughness. We show that the roughness allows to tune the friction coefficient by more than an order of magnitude, which can be explained completely by a simple geometrical model. A Kirigami metamaterial surface allows us to show that this understanding of geometrical friction can be used to externally control the friction in a single system by externally controlling its roughness.

6.1 Introduction

The resistance to sliding of objects is experienced daily, but remains ill-understood. The friction force is often specific to the conditions and, therefore, hard to predict. Various parameters such as geometry, load or surface roughness can alter the sliding friction significantly. Often, low friction is desired in biological and industrial tribological systems; it has been estimated that a third of the world energy consumption is spent on friction and, therefore, a better understanding of it would have a large impact [1]. In contrast, high friction can be beneficial as well; the rubber of a shoe on the pavement or a finger on a tennis racket desire high grip and no slip [135, 136]. A good control of friction is therefore of interest in many applications: high friction for grip and low friction for easy sliding. We show here that direct control may be achieved by controlling the (macroscopic) surface topography.

Surface roughness alters the friction force significantly; in general the larger the roughness, the larger the friction. However, the precise influence of the local surface height variation on the friction is hard to predict and control [137–140]. Often a combination of abrasion (wear, plastic deformation) [48, 141, 142], interlocking [143,144], and squeezing out the lubricant if present [37,145,146] are the main reasons for the increase of friction. At the nanoscale, the potential of controlling friction by surface topography has been shown previously [52, 53, 147–149]. Depending on the commensurability of periodic nanoscale surfaces, the friction force can be modified to extremely low values. This so-called structural lubricity enables the friction force to be controlled over a large domain based on the (in)commensurability of surface roughness [44]. In this chapter, we explore the ability to modify the friction force with macroscopic periodic surface roughness on custom-made surfaces. We show that the friction force for a dry and rigid system can be modified based on well-designed periodic surface roughness.

The use of artificial manufactured surface roughness, or surface patterning, is well established. The ridges on a bottle of water [150] or the grooves in an anti-slip floor surface [151] are designed to increase the grip. These millimetre-size ridges and grooves give the opportunity to squeeze out any (slippery) liquid and, by elastic deformation of the surfaces, they interlock which results in grip. In contrast, surface patterning on the sub-millimetre scale can be manufactured on bearing-shafts to increase the slipperiness: The surface patterning increases the durability of the lubricated system as it entraps wear debris and can act as a lubricant reservoir [152]. However, controlled friction in dry systems based on designed surface roughness is often limited by wear and rigidity.

Based on (digital) fabrication techniques, we design macroscopic roughness on rigid surfaces and measure the friction to slide one patterned surface over the other. With direct control on the (in)commensurability and slope of the periodic surface height variation, we manage to vary the friction force by more than an order of magnitude. In addition, we show that with Kirigami metamaterial surfaces the periodic surface roughness can be varied externally which, subsequently, enables direct control of the sliding friction.

6.2 Experiments

6.2.1 Sawtooth patterned surfaces

We perform sliding experiments with geometrically controlled surfaces to monitor the influence of macroscopic periodic roughness on the friction force. One of the designed surface patterns is the so-called *sawtooth*-pattern: a macroscopic periodic roughness that is based on a row of identical triangular prisms. The prisms are based on isosceles triangles with a controlled interior angle θ and depth of 20 mm. For a fixed height h of 3 mm, we fabricate the sawtooth pattern as macroscopic surface patterning for over a length of 60 mm. The top surface is pulled over a bottom surface where, for simplicity, the top surface pattern is present as a single sawtooth.

The macroscopic periodic roughness is fabricated on the surfaces of plastic, aluminium, and stainless steel objects; see also Table 6.1. The plastic surfaces are manufactured with digital fabrication techniques. A commercially available resin, named *Clear*, is 3D printed with the Form 3 (Formlabs). Based on stereolithogra-

Material name	Material type	Fabrication technique	Resolution (μm)	Roughness (μm)
Plastic	Clear	Stereolithography	25.0	3.454
Aluminium	6082-T6	Wire electrical discharge	5.0	0.705
Stainless steel	AISI 316	Wire electrical discharge	5.0	0.470
Kirigami	Mylar	Laser cutting (2.0″ lens)	1.0	0.073

Table 6.1: Details of the materials used for the custom-made surfaces. The listed resolutions are for the fabrication of flat surfaces. The listed roughness S_q is the root-mean-square surface height variation which is quantified as described in Section 2.3.

Material	Patterning	Gravitational force F_G (N)	Friction coefficient μ_0 (-)
Aluminium	Sawtooth	1.18, 1.67, 2.69	0.23 ± 0.02
Aluminium on stainless steel	Sawtooth	1.18, 1.67, 2.69	0.21 ± 0.02
Stainless steel	Sawtooth	1.53, 2.03, 3.00	0.18 ± 0.03
Plastic	Sawtooth	0.61, 1.10, 2.09	0.12 ± 0.01
Plastic	Sinusoidal 1D	0.61, 1.10, 2.09	0.12 ± 0.01
Plastic	Sinusoidal 2D	0.85, 1.34, 2.32	0.12 ± 0.01
Plastic on Kirigami	Sawtooth on Kirigami	0.32, 0.61, 1.10	0.20 ± 0.01

Table 6.2: Details of the sliding experiments performed for the various materials and surface patterns. The gravitational force F_G is controlled by placing dead weights on the slider. The listed microscopic friction coefficient μ_0 is the measured coefficient without the patterning, i.e., the plate-on-plate friction coefficient.

phy, the liquid resin is cured into hardened plastic by photopolymerization with a print-resolution (both axis and lateral) of 25 μm [153]. For the aluminium (6082-T6 aluminium alloy) and stainless steel (AISI 316) surfaces, wire electrical discharge machining is used; the patterning is fabricated by removing material with electrical discharges (sparks) from a 0.25 mm brass wire. This technique has a resolution of 5.0 μm for the fabrication of *mm*-size macroscopic surface roughness. However, the resolution of this technique is significantly less for the fabrication of high surface slopes in μm-size surface patterns. The microscopic surface topography — the microscopic surface roughness — of all materials is measured prior to sliding by laser-scanning profilometry as described in Section 2.3. The calculated root-mean-square surface height variation S_q is listed in Table 6.1.

The sliding experiments are performed with the custom-made horizontal sliding setup as introduced in Chapter 2; we pull the top surface horizontally at an imposed constant sliding speed of 1 mm/s over the bottom surface. The pulling force F_T is monitored as a function of the sliding distance d while the gravitational force F_G is controlled by placing dead weights on the slider; see Table 6.2.

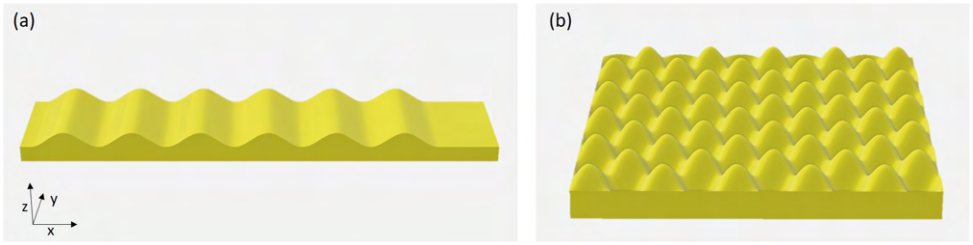

Figure 6.1: Designs for the 1D (a) and 2D (b) sinusoidal patterned surfaces. The height Z of the surface is defined by Equations (6.1) and (6.4).

6.2.2 Sinusoidal patterned surfaces

In order to study the influence of commensurability, we also design a sinusoidal pattern, 3D printed with the hardened resin *Clear*, with a length and width of, respectively, 60 mm and 20 mm (which are the same as for the sawtooth patterned surfaces). The height profile Z is defined as

$$Z(x) = b \sin(\frac{2\pi}{a}x) \,, \tag{6.1}$$

with b the amplitude and a the wavelength; see Figure 6.1(a) for the design. The angle θ of this sinusoidal patterning can be defined based on the surface slope $\tan(\theta) = \frac{\partial Z}{\partial x}$ which can be written as

$$\theta = \tan^{-1}\left(\frac{2\pi}{a} b \cos(\frac{2\pi}{a}x)\right) \,. \tag{6.2}$$

Consequently, the maximum angle of the surface pattern is:

$$\theta_{\text{max}} = \tan^{-1}\left(\frac{2\pi b}{a}\right) \,. \tag{6.3}$$

The manufactured top surface has a wavelength of $a_{\text{top}} = 5.44$ mm and amplitude $b = 1.5$ mm which results in $\theta_{\text{max}} = 60°$. Several bottom surfaces are fabricated with wavelengths starting from $a_{\text{bottom}}/a_{\text{top}} = 0.8$ up to $a_{\text{bottom}}/a_{\text{top}} = 2.4$ with a constant amplitude b of 1.5 mm.

In addition, surfaces with a macroscopic periodic roughness in 2D are fabricated, as can be seen in Figure 6.1(b). The height Z can be described as

$$Z(x,y) = b_{\text{x}} \sin(\frac{2\pi}{a_{\text{x}}}x)\; b_{\text{y}} \sin(\frac{2\pi}{a_{\text{y}}}y) \,, \tag{6.4}$$

with $a_x = a_y = 10.88$ mm, and $b_x = b_y = \sqrt{3}$ mm which results in a maximum patterning angle of $\theta_{max} = 60°$. The top and bottom surfaces have the same patterning with 5 periods in the x and y direction. For both sinusoidal patterns, the pulling force F_T are measured for sliding horizontally at a preset sliding speed of 1 mm/s for various applied gravitational forces F_G; see Table 6.2.

6.2.3 Kirigami metamaterial

We perform sliding tests in which a sawtooth patterned top surface slides on a Kirigami metamaterial surface. Kirigami is the Japanese artform of paper cutting where, with a well-designed pattern, the flat sheet reforms in a 3D structure while stretching out. We laser-cut a pattern in a Mylar sheet that has a thickness of 125 μm, a width of 50.67 mm, and a length of 85 mm. As design we use a triangular pattern, see Figure 6.2. This patterning is based on an array of unit cells (see the black lines in Fig. 6.2) where the unit cell is a rhombus; a quadrilateral where all four sides have the same length l_0. Two straight cuts (red line in Fig. 6.2) along the sides of the unit

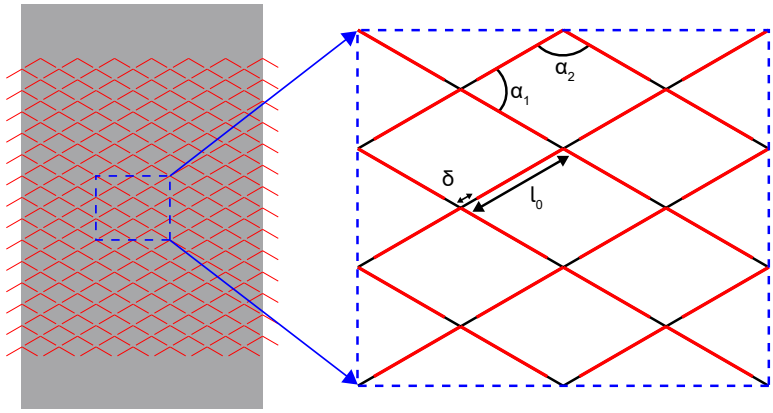

Figure 6.2: Design for the Kirigami metamaterial surface made with a 125 μm thin Mylar (polyethylene) sheet, see the gray area. The red lines represent the cuts fabricated in the sheet; the periodic patterning is based on a unit cell that is arranged in a triangular lattice. The unit cell (black lines) is a rhombus, the four sides have a length $l_0 = 4.5$ mm and the interior angles are $\alpha_1 = 60°$ and $\alpha_2 = 120°$. Two straight cuts, as represented by red lines, are made along the top two sides and, therefore, connect at the top and leave a length of $\delta = 0.7$ mm intact.

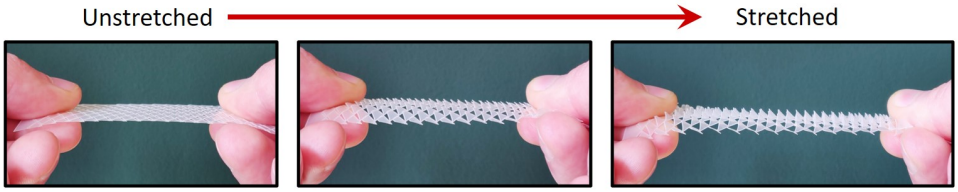

Figure 6.3: A fabricated Kirigami metamaterial surface. When the thin sheet is stretched uniaxially, the surface exhibits a roughness which consists of triangular scales pointing out-of-plane.

cell were made which are connected at the top corner and leave a length δ intact. Inspired by Reference [154], we design the Kirigami pattern with interior angles of the unit cell of $\alpha_1 = 60°$ and $\alpha_2 = 120°$, side length of $l_0 = 4.5$ mm and cuts with a length of 3.8 mm ($\delta = 0.7$ mm). The patterning is made along the full width of the sheet and for a length of $L_0 = 63.08$ mm.

The Kirigami sheets exhibit an out-of-plane roughness when stretched uniaxially; triangular 'scales' are formed where the height of the formed roughness can be amplified with the set strain as can be seen in Figure 6.3. In the sliding experiments, we have clamped both long sides of the Kirigami patterned sheet and, with the use of a micro-screw, stretch it uniaxially up to a length L. Consequently, we monitor the strain ϵ which is defined as

$$\epsilon := \frac{L - L_0}{L_0} , \tag{6.5}$$

where L and L_0 are, respectively, the deformed and undeformed length of the Kirigami patterned part of the surface. For a set strain, we quantify the horizontal pull force F_T when sliding against and along the formed Kirigami-scales at various applied gravitational forces F_G, see Table 6.2.

6.3 Results

6.3.1 Macroscopic periodic roughness controls friction

Experimental results

We start by discussing the results for the *sawtooth* patterned surfaces. A top surface with a single triangular prism is slid horizontally over a surface with the designed sawtooth pattern [Fig. 6.4(a) top]. The pulling force F_T as a function of the sliding distance d is monitored which results in a square-wave function [Fig. 6.4(a) bottom]. When the slider moves uphill over the bottom surface, a high and constant tangential force is measured. Subsequently, when the top of the sawtooth pattern is reached, the force drops and a constant (negative) force is found up until the slider is back down again.

The plateau values F_{max} and F_{min} for, respectively, uphill and downhill sliding

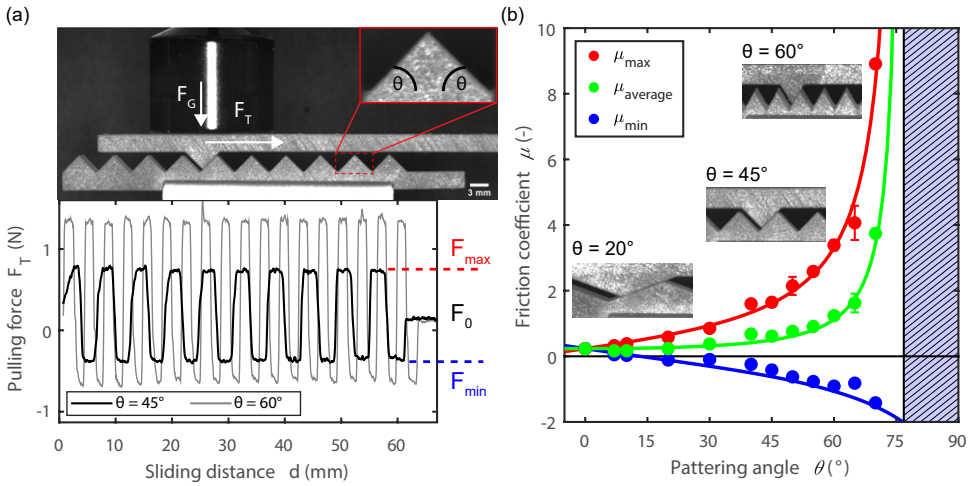

Figure 6.4: Sliding experiments with sawtooth patterned surfaces. (a) Experimental setup visualised from the side of the sliding experiment and the monitored pulling force F_T as a function of distance d. As macroscopic roughness, a sawtooth pattern is fabricated with a fixed height of 3 mm and controlled angle θ. The observed square wave of the pulling force is shown for $\theta = 45°$ and $\theta = 60°$ in, respectively, black and gray. (b) Friction coefficient μ as a function of the angle θ for the maximum (red), average (green) and minimum (blue) friction, either measured (circles) or calculated (continuous lines) with Eqs. (6.8) to (6.10).

are set by the angle θ of the sawtooth pattern. The magnitude of both $F_{\max}$ and $F_{\min}$ increase when the patterning angle θ increase. In Figure 6.4(b) the influence of the angle θ is observed for maximum (red), minimum (blue) and average (green) macroscopic friction coefficient μ which is defined as the ratio of the measured tangential to the normal (gravitational) force. The gravitational force F_G is given by the mass of the dead weights on top of the slider and the slider itself, see Table 6.2. The friction depends strongly on the angle θ of the macroscopic periodic roughness of the sliders; for example, the maximum friction coefficient for $\theta = 60°$ is $\mu_{\max} = 3.4$. Furthermore, the average friction coefficient can increase by more than an order of magnitude when the patterning angle θ is varied from 20° to 60°.

A simple geometrical model for the measured sliding friction

The significant influence of the angle θ on the friction coefficient can be understood by considering the force balance, illustrated in Figure 6.5. The maximum macroscopic friction coefficient, defined as the ratio of tangential to gravitational force, can be written as

$$\begin{aligned} \mu_{\max} &= \frac{F_T}{F_G} \\ &= \frac{F_N \sin(\theta) + F_F \cos(\theta)}{F_N \cos(\theta) - F_F \sin(\theta)} , \end{aligned} \tag{6.6}$$

where F_N and F_F are, respectively, the normal and friction force for sliding the patterned top surface uphill. In the uphill direction, the friction force is set by the microscopic friction coefficient μ_0: $F_F = \mu_0 F_N$. The microscopic friction coefficient is measured during flat-on-flat sliding, i.e., $\theta = 0°$, with the same materials under the same conditions and is found to be 0.23 ± 0.02 for the aluminium sliders; see Table 6.2. Alternatively, this flat-on-flat friction coefficient can be derived from the tilt angle θ_0. A flat surface will continuously slide over a tilted bottom surface for a minimum angle θ_0 which results in a definition of the microscopic friction coefficient of

$$\mu_0 = \tan(\theta_0) . \tag{6.7}$$

Note that the tilt angle here is defined for the dynamic sliding condition. For the quantification of the static macroscopic friction coefficient, we expect that the related static tilt angle can be used that is defined based on the — slightly higher — static friction coefficient. Consequently, Equation (6.6) can be rewritten in terms of the microscopic angle θ_0:

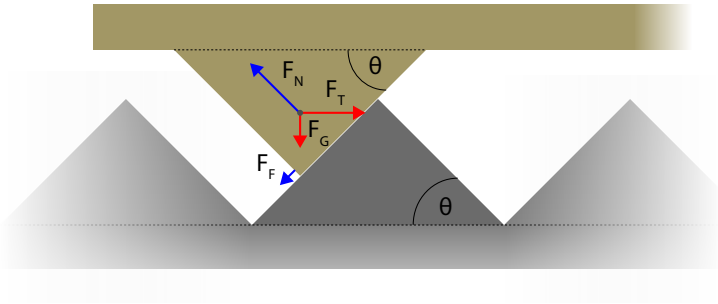

Figure 6.5: Schematic illustration, including a force balance, for sliding two sawtooth patterned surfaces with patterning angle θ over each other. F_G is the gravitational force, F_N the normal force, F_F the friction force and F_T the horizontal pulling force.

$$\mu_{max} = \tan(\theta + \theta_0) \, . \tag{6.8}$$

Similar to the maximum friction coefficient, the minimum friction coefficient can be derived likewise where the patterning angle is negative:

$$\mu_{min} = \tan(-\theta + \theta_0) \, . \tag{6.9}$$

Furthermore, the average macroscopic friction coefficient is

$$\mu_{average} = \frac{\tan(\theta + \theta_0) + \tan(-\theta + \theta_0)}{2} \, . \tag{6.10}$$

In Figure 6.4 the model is shown as the continuous lines and captures the frictional behaviour of sawtooth patterned surfaces. The measured microscopic friction coefficient μ_0 for the aluminium sliders was used to calculate the microscopic angle $\theta_0 = 13°$ [Table 6.2 and Eq. (6.7)]. The blue dashed area in Figure 6.4 represents the zone which is experimentally unreachable; due to the nonzero microscopic angle θ_0 of the surface, the macroscopic friction coefficient reaches infinity at the critical angle $\theta_c = 90 - \theta_0 = 77°$. Above this critical angle, the interlocking of the surfaces results in suppressing the sliding motion.

The friction can therefore be modelled based on the patterning angle θ of the macroscopic periodic surface roughness, and the microscopic sliding friction which can be represented with the microscopic angle θ_0 of the sliders. The latter can be varied by using different slider materials (see Table 6.1) which indeed have various microscopic friction coefficients μ_0 as listed in Table 6.2. These materials, aluminium

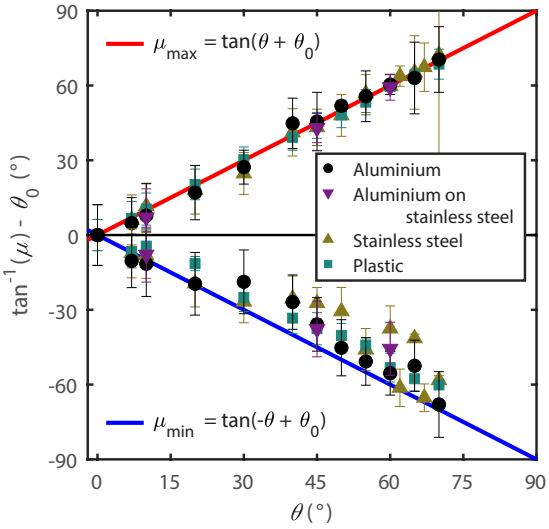

Figure 6.6: The maximum and minimum friction coefficient, normalised with the material-specific angle $\theta_0 = \tan^{-1}(\mu_0)$ where μ_0 is the microscopic friction coefficient, for increasing angle θ. For various materials, aluminium, aluminium on stainless steel, stainless steel, and plastic sliders (more details listed in Table 6.1) the sliding experiments are performed (see Table 6.2 for more details). The red and blue continuous lines represent, respectively, the calculated maximum [Eq. (6.8)] and minimum [Eq. (6.9)] friction coefficient.

stainless steel, and plastic, all exhibit the expected increase in friction as a function of the angles θ_0 and θ. In Figure 6.6, the measured maximum and minimum friction coefficient, normalised with the material-dependent angle θ_0, are given for increasing patterning angle θ. In addition, we plot $\mu_{\max}$ and $\mu_{\min}$ (continuous lines) calculated from the model that indeed predicts the measured friction. A systematic deviation between the measurements and the calculation for $\mu_{\min}$ can be observed; we interpret this deviation as a result of a tilt of the slider when it slides down along the sawtooth pattern. The rod pulling on the slider and attached to the stepper motor is compressed when sliding down because of the negative force. Consequently, the rod will slightly buckle which allows the slider to tilt and thereby decreasing its effective angle θ during sliding down the sawtooth pattern.

Size of the macroscopic periodic roughness

We have shown that the friction can be tuned with a designed periodic roughness and can be modelled based on the angle θ of the roughness and the microscopic friction coefficient μ_0 of the sliding surfaces. The measured, and designed, friction coefficient of the sawtooth patterned surfaces is, however, not entirely independent of the height of the patterns. Decreasing the height of the designed sawtooth's from 3 mm down to the μm scale would offer the opportunity to implement the tuning of the friction in various tribological applications; lifting up and down the top surface for 3 mm is for many sliding systems impractical. The potential of (periodic) roughness on the μm scale to improve the often-lubricated tribological performance is already known [152]. Artificial roughness can eliminate the influence of wear debris, controls the contact area or improve a lubricated sliding system [152,155–157]. We therefore quantify the influence of the height of the surface patterns on the sliding friction and find that, unfortunately, the resolution of the fabrication technique limits the ability to tune the friction for small-scale sawtooth patterned surfaces.

The pulling force for an aluminium top surface with a single sawtooth, height of 3 mm and angle θ_T of 45°, is measured when sliding over an aluminium surface with decreasing patterning height; see Figure 6.7. We observe plateaus in the measured pulling force when sliding up and down the patterning for approximately the first

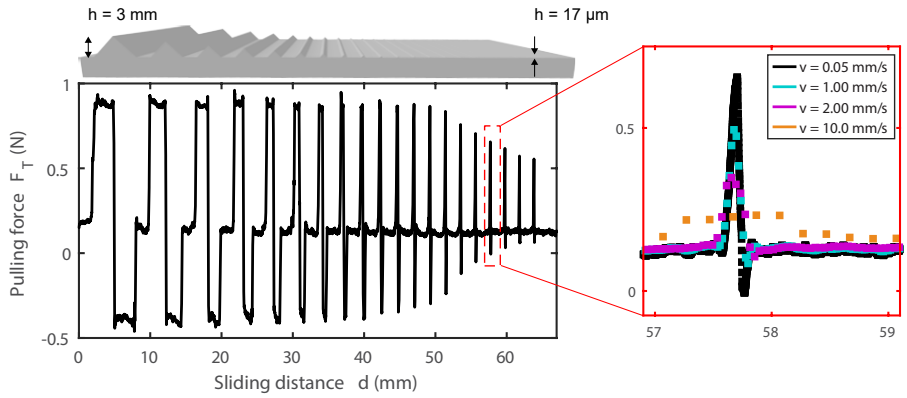

Figure 6.7: Pulling force F_T as a function of the sliding distance d for a sawtooth patterned ($\theta = 45°$) surface fabricated in aluminium with a stepwise decreasing height h. The sliding speed is set at $v = 0.05$ mm/s for an imposed gravitational load of $F_G = 0.72$ N. On the right, the measured pulling force for sliding over a single sawtooth pattern is given for various sliding speed.

8 teeth. However, for the smaller sawtooth's with heights down to 17 μm, only peaks in the pulling force are found. To increase the resolution of the monitored friction force, the sliding speed is decreased down to 0.05 mm/s. In Figure 6.7 the effect of speed is shown for sliding over a single sawtooth. As the sampling frequency of the tensile tester is 50 Hz, the sliding distance per datapoint increases from 1 μm/datapoint to 200 μm/datapoint for respectively 0.05 mm/s and 10 mm/s.

We calculate the maximum friction coefficient as a function of the patterning height h, shown as red circles in Figure 6.8(a). The continuous line represents the maximum friction coefficient based on the geometrical model [Eq. (6.8)]. As expected, the sliding friction for a sawtooth pattern with a height of 3 mm is in agreement with the model. However, a significant decrease of the sliding friction is observed when the height of the sawtooth is smaller than 200 μm. This can be explained

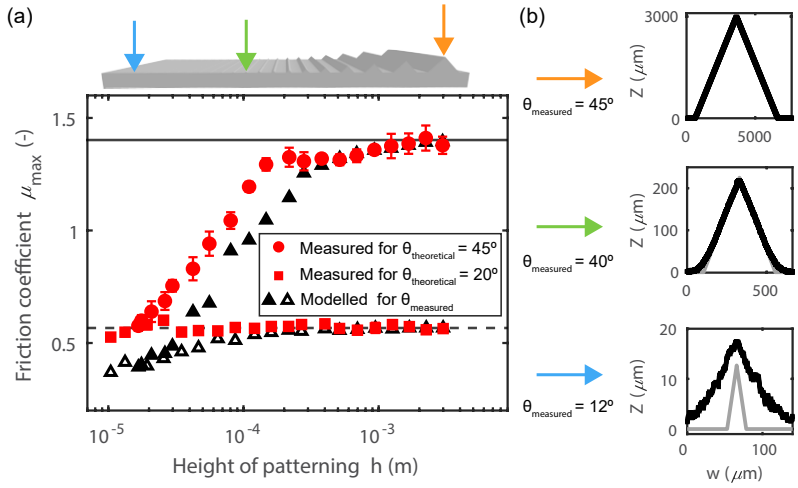

Figure 6.8: (a) Friction coefficient μ for sliding on a sawtooth patterned surface as a function of the pattern height h. The measured maximum friction coefficient is presented as circles and squares for surfaces where patterning angle $\theta_{\text{theoretical}}$ was attempted to hold constant at, respectively, 45° and 20°. The lines show the theoretical friction coefficient μ_{max} [Eq. (6.8)]. As a result of the limited resolution of the fabrication technique, the angle θ decreases significantly for decreasing patterning height. The black triangles are the friction coefficient μ_{max} calculated based on the measured angle θ_{measured}. (b) The line profiles, the height Z as a function of the width, for three sawtooth patterns with decreasing height. The black line represents the measured line profile where the gray line shows the profile that was attempted to be fabricated. The angle θ_{measured} can be quantified based on the slope of the line profiles.

with the limited resolution of the fabrication technique. When an angle $\theta = 45°$ is aimed for, the actual angle is smaller when the patterns are small. We characterise the angles of the manufactured sawtooth patterned surfaces with 3D laser-scanning profilometry (see Section 2.3 for more details) prior to the sliding test. In Figure 6.8(b) the measured height profile Z as a function of the width w is given, shown as black continuous line for three sawtooth patterns with decreasing height. Indeed, for a sawtooth with a height of 3 mm, the angle is 45° as can be calculated based on the slope of the measured height profile. However, the angle decreases to 40° when the height is lowered to 218 μm and gradually decreases further to 12° for a patterning height of 17 μm. Based on the measured angle θ_{measured} for a given height of the sawtooth pattern, the expected maximum friction coefficient μ_{max} can be calculated [Eq. (6.8)] and is given in Figure 6.8 as the black-filled triangles. This is in reasonable agreement with the measured sliding friction and, therefore, explains that when a high angle of 45° can not be achieved for sub-mm patterning, the sliding friction decreases. The influence of the limited fabrication resolution is smaller when a smaller angle θ is designed; the red squares in Figure 6.8 represent the measured maximum friction coefficient for a sawtooth patterned surface with an angle of 20°. Up to a height of 35 μm the patterning can be fabricated with only a small decrease of the angle down to 15°.

Although the decrease of friction for decreasing height of the patterning can be qualitatively explained with the decrease in the fabricated angle θ, full agreement between the measured and calculated friction coefficient is not achieved. We interpret this discrepancy as a result of the surface roughness on the sawtooth pattern; the 3 mm high sawtooth has the expected root-mean-square surface roughness of $S_{\text{q}} = 0.705$ μm (Table 6.1) where, however, the smallest designed sawtooth (a height of 17 μm) has an increased roughness of $S_{\text{q}} = 1.695$ μm (measured for a limited area of 32.7 μm by 208 μm). The increase of surface roughness could explain the underestimation of the friction coefficient of, on average, 0.21 for the model compared with the data of $\theta = 45°$ for patterning heights lower than 200 μm. We therefore suggest that the increased roughness results also in an increased microscopic friction coefficient μ_0 which, in general, for flat-on-flat sliding experiments can be expected; two rough surfaces slide less easy over each other than two smooth ones.

We can therefore decrease the height of the designed periodic surface roughness to tune friction, but the fabrication technique limits the design. We interpret the observed decrease of the maximum friction coefficient for surface patterns below a height of 200 μm as a result of not reaching the high target angle θ. The decrease of friction for decreasing patterning height is partly compensated with the increase in

surface roughness. We therefore would expect that with an increase of the fabrication precision the tuning of friction could also be performed for smaller patterns.

6.3.2 (In)commensurability of macroscopic periodic roughness

In reality two surfaces are rarely commensurable, and it is therefore interesting to study the sliding friction of incommensurable surfaces. Perhaps the most interesting observation is that when the sliders are incommensurable, the sliding friction is controlled by the lowest angle θ of the two related surfaces. In Figure 6.9 (in)commensurable sawtooth patterned surfaces are shown; in (a) the friction coefficient is plotted for increasing angle of the top surface θ_T when sliding over a surface with a set angle $\theta_B = 45°$. In the domain $\theta_T < \theta_B$, the measured friction varies with the angle θ_T and agrees with the model [Eqs. (6.8) to (6.10)]. However, for $\theta_T > \theta_B$

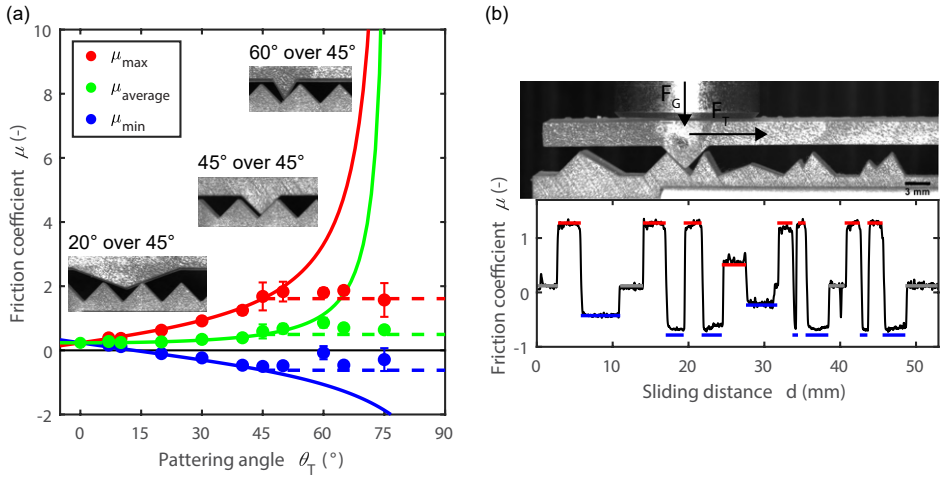

Figure 6.9: (a) Friction coefficient μ as a function of the patterning angle θ_T of the top surface which is pulled over a surface with a constant patterning angle of $\theta_B = 45°$. The maximum, average and minimum friction coefficient are represented in, respectively, red, green, and blue. The observed sliding friction is set by the lowest angle of the top and bottom surface. The continuous lines and dashed lines represents the expected friction based on, respectively, θ_T and θ_B [Eqs. (6.8) to (6.10)]. (b) Friction coefficient μ for sliding on a surface with a quasi-random surface roughness as a function of the sliding distance d. The sliding friction can be predicted based on the lowest angle of the top and bottom surface (continuous lines).

the friction remains constant and is set by the patterning angle of the bottom surface; the horizontal dashed lines represent the expected friction coefficient for a constant angle $\theta_B = 45°$ [Eqs. (6.8) to (6.10)]. This suggests that sliding on a surface with a quasi-randomly macroscopic surface roughness can be understood based on the lowest angle of the two surfaces. As an example, we perform a sliding experiment on a quasi-random patterned surface; see Figure 6.9(b). We slide a top surface with $\theta_T = 45°$ over this designed surface and plot the friction coefficient as a function of the sliding distance d together with the calculated friction coefficient based on the lowest angle of the two surfaces. The model is indeed in agreement with the measured sliding friction coefficient and show that the maximum tuning is limited by the top surface; although sliding over a high angle as $\theta_B = 60°$, the maximum friction is set by the top surface with $\theta_T = 45°$.

Incommensurability therefore restricts the domain of tuning; the friction is set by the lowest angle of the macroscopic roughness of the surfaces. The influence of mismatching surfaces is not restricted to sawtooth patterned surfaces. In Figure 6.10(a) the influence of commensurability is shown for sliding surfaces with a sinusoidal patterned surface. The height Z of the sinusoidal pattern is designed with a controlled wavelength a and a fixed amplitude $b = 1.5$ mm [Eq. (6.1)]. A top surface, which contains 6 periods with a set wavelength ($a_{top} = 5.44$ mm), is pushed over several bottom surfaces where the wavelengths a_{bottom} is varied. We observe a peak in the friction coefficient when the two surfaces have a commensurable periodicity of surface patterns: $a_{bottom}/a_{top} = 1$ and 2. The increase of friction is the result of a matching periodicity of the patterns; when the surfaces fit into each other, the high surface angle θ of the sinusoidal patterning can be reached and increases the sliding friction. The maximum, minimum, and average friction coefficient for commensurable sliding can be calculated based on the simple geometrical model [Eqs. (6.8) to (6.10)] and the angle θ of the sinusoidal patterned surfaces [Eq. 6.3]. The model, represented as the open circles in Figure 6.10, matches the measured sliding friction. Note that the tuning of the friction coefficient is limited when high ratios a_{bottom}/a_{top} are set; the maximum angle θ_{max} of the sinusoidal surfaces decreases for increasing wavelength a_{bottom}. Tuning with commensurable sinusoidal surfaces is therefore possible, although for higher ratios a_{bottom}/a_{top} limited due to the significant decrease of the angle θ. When the two sinusoidal surfaces are incommensurable, we observe a decrease of the sliding friction. When the designed surfaces do not fit into each other, and therefore the surface angles θ in contact are small, the resulting sliding friction is low. The average friction coefficient converges to the lowest limit for these sliding surfaces: the microscopic friction coefficient, i.e., the flat-on-flat

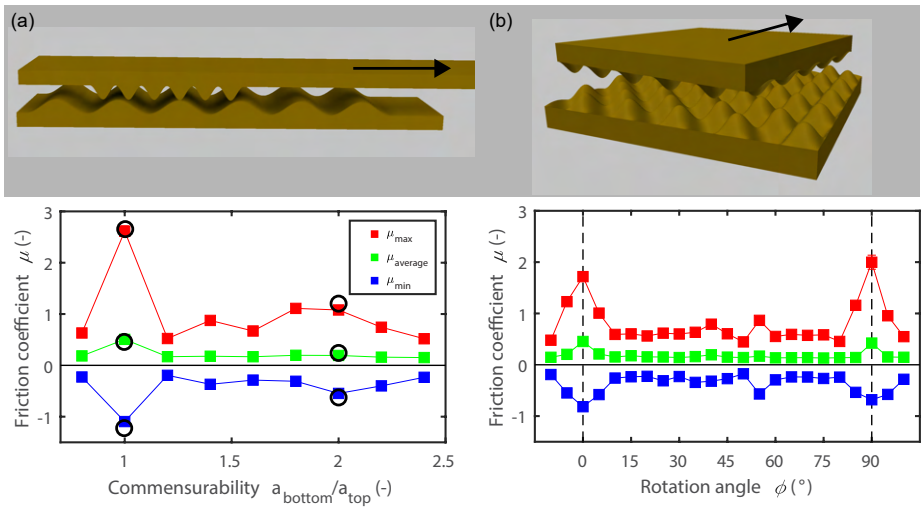

Figure 6.10: Friction coefficient μ for 1D and 2D patterned surfaces as a function of the commensurability. (a) The sliding friction as a function of the ratio of wavelengths of the 1D sinusoidal patterned surfaces. The open circles show the friction coefficient expected for full-commensurable sinusoidal patterned surfaces (at $a_{\text{bottom}}/a_{\text{top}} = 1$ and 2 based on Eq. (6.3). (b) The sliding friction as a function of the rotation angle ϕ between the 2D sinusoidal patterned surfaces.

sliding friction $\mu_0 = 0.12$.

A similar influence of commensurability has been observed in nanotribology and is called structural lubricity: the friction force approaches zero when sliding two atomically incommensurable surfaces over each other [52, 158–160]. The structural superlubricity of two graphite surfaces has been shown by Dienwiebel et al. [52]. Graphite has an atomic hill-and-valley landscape in a hexagonal manner which, when rotated, only is commensurable every 60°. The graphite-on-graphite friction reaches ultralow values which, when rotated, shortly increases every 60°. In Figure 6.10(b), we show that structural lubricity is not limited to the microscale; 2D macroscopic surface roughness based on a hill-and-valley landscape [see Eq. (6.4)] permits control on the friction coefficient through the rotation angle ϕ. We perform sliding experiments with the custom-made 2D patterned surfaces and measure the sliding friction as a function of the rotation angle ϕ between the two surfaces. Only when the surfaces are in registry, i.e., at $\phi = 0°$ and every following 90° rotation, a high friction coefficient can be observed. Similarly as to what was observed for the 1D sinusoidal patterned surfaces, the friction coefficient decreases when rotated out

of registry.

In general, tuning sliding friction is limited when the designed surfaces are incommensurable. However, with the use of 2D macroscopic surface patterns, the commensurability can be controlled with the rotation of the sliding surface and, subsequently, the sliding friction can be tuned. We continue the exploration of tuning (asymmetric) sliding friction with external parameters with sliding on a Kirigami metamaterial surface. This patterned surface allows us to control the surfaces roughness externally by applying a tensile stress.

6.3.3 Sliding friction on a Kirigami metamaterial

Tuning friction with macroscopic surface topography does also facilitate asymmetric sliding friction; an asymmetry in the surface patterning can result in a different sliding friction based on the sliding direction [161, 162]. With the use of Kirigami metamaterial surfaces, the surface roughness can be controlled externally which results in an asymmetric surface patterning and, consequently, an asymmetric sliding friction [163, 164]. Kirigami is a Japanese artform of paper cutting where, with repetitive patterns, highly stretchable and 3D objects can be achieved from a flat sheet [165–167]. With a well-designed patterning of cuts, out-of-plane texturing can be formed for increasing in-plane uniaxial strain. Rafsanjani et al. made use of this technique to tune on-demand the texturing of a Kirigami metamaterial sheet [154]. The authors designed a bioinspired 'snake' that, due to repeated stretching and releasing of the Kirigami skin, can crawl forward; this is indeed very similar to the scaled skin of snakes which enable them to propel themselves [168, 169]. This metamaterial crawler was fabricated by attaching a Kirigami-pattered sheet to the surface of a soft cylindrical actuator that extends axially upon inflation. When inflated, the Kirigami skin, due to the increase of strain, forms an out-of-plane texturing. The formed texture interlocks at the rough substrate where it is placed on and, with cycled inflation, the crawler performs locomotion. The formation of on-demand texturing, based on Kirigami 'scales' point out-of-plane, is very similar to the sawtooth patterns. Therefore, in addition to interlocking due to the formation of anchoring points, the Kirigami metamaterial surface does allow tuning the friction by externally controlling its roughness.

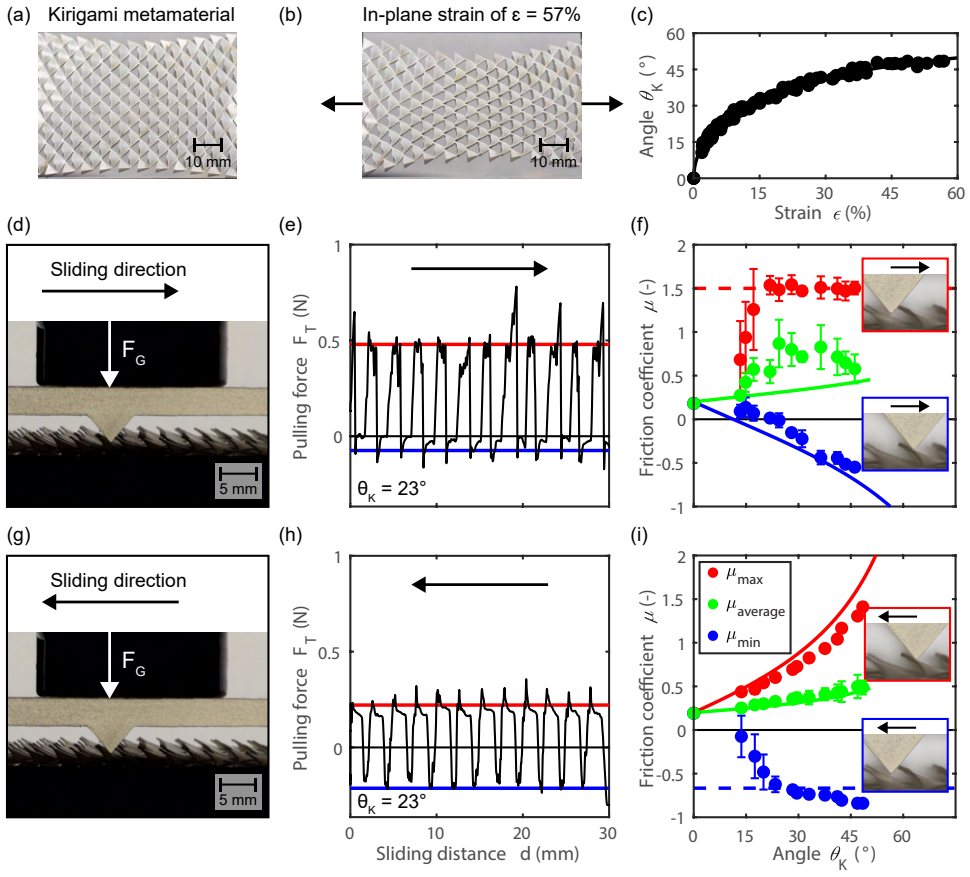

Figure 6.11: Sliding experiments on a Kirigami metamaterial. (a) A Kirigami patterning is laser-cut in a Mylar sheet. (b) A macroscopic out-of-plane surface roughness, i.e., scales pointing outwards, can be actuated for increasing in-plane uniaxial strain ϵ. (c) Kirigami angle θ_K for increasing strain ϵ. The black continuous line is a fit, see Appendix B.1 for more details. (d) Side-view of the sliding experiment when sliding against the formed Kirigami scales. The slider has a single sawtooth pattern with an angle of $\theta_T = 45°$. (e) Pulling force F_T as a function of the sliding distance d when the slider is pulled against the Kirigami scales pointing upward with an angle of $\theta_K = 23°$. In continuous red and blue lines, the calculated friction coefficient for, respectively, the maximum [Eq. (6.8)] and minimum [Eq. (6.8)]. (f) Friction coefficient μ as a function of the measured Kirigami angle θ_K for sliding against the scales. In continuous lines the calculated friction coefficients are shown [Eqs. (6.8), (6.9), and (B.2)]. (g-i) The sliding experiment when performed along the Kirigami scales.

To demonstrate the capability of Kirigami metamaterials to tune the friction, we laser cut a Mylar sheet with a triangular pattern (see Section 6.2 for more experimental details) and perform sliding experiments while controlling the in-plane uniaxial strain ϵ. In Figure 6.11(a) and (b) we visualise from top the response of the Kirigami metamaterial for increasing strain. The scales point upwards with an angle θ_K that can be quantified visually from the side; see Figure 6.11(c). We perform sliding experiments with a single sawtooth ($\theta_T = 45°$) patterned plastic surface pulled horizontally against and along the Kirigami scales as visualised in, respectively, Figure 6.11(d) and (g). The pulling force F_T for sliding on the Kirigami surface, at a controlled angle of $\theta_K = 23°$, as a function of the sliding distance is given in Figure 6.11(e) and (h) for, respectively, sliding against and along the scales. The measured pulling forces indeed roughly have a square wave shape, similarly as was found for the sawtooth patterned surfaces. The square wave is disturbed by periodic peaks in the pulling force, located when the slider reaches the top of the Kirigami scales. The end of the Kirigami scale acts as an anchoring point, i.e., it grips the top surface. Only when the pulling force has been sufficiently increased, the slider jumps over the scale and the interlocking is released. With the remaining plateaus in the square wave, that can again be quantified with F_{max} and F_{min}, the upward and downward macroscopic friction coefficient can be calculated for the set gravitational force F_G.

In Figure 6.11(f) and (i), the maximum, minimum, and average friction coefficient is given as a function of θ_K when sliding against and along the Kirigami scales. Similar as for the sawtooth patterned sliders, the maximum and minimum friction coefficient can be modelled with Equations (6.8) and (6.9), shown as the red and blue continuous lines. Again, the smallest angle θ, that is either the Kirigami scale angle θ_K or the angle of the top surface θ_T, sets the friction coefficient. The measured maximum and minimum friction coefficient is, therefore, very anisotropic: it depends on the sliding direction and shows strongly asymmetric friction.

In addition, the measured average friction coefficient [shown as the green circles in Fig. 6.11(f)] is very high and seems to be rather θ_K-independent when sliding against the pattern. It increases smoothly with θ_K when sliding with the pattern, shown as the green circles in Figure 6.11(i). The high and rather constant value of the friction when sliding against the pattern is likely due to sticking of the material on the top. This asymmetry of the Kirigami metamaterial decreases with increasing strain and can be geometrically calculated, as discussed in Appendix B.1. The green lines in Figure 6.11(f) and (i) are the weighted average friction coefficient based on the asymmetric path lengths [respectively Eqs. (B.2) and (B.3)].

Kirigami metamaterial surfaces, or even metamaterials in general [170], allows us to control the sliding friction externally based on the formation of 3D texturing. Next to the asymmetric friction based on interlocking, a Kirigami metamaterial does also facilitate sliding friction with an on-demand tunable friction coefficient.

6.4 Discussion and conclusion

We have presented sliding experiments of sliders with various macroscopic surface patterning and shown the influence of the patterning slope and the commensurability of the surfaces. A simple geometrical model describes the measured sliding friction based on the macroscopic geometry together with the microscopic friction coefficient μ_0. The influence of macroscopic geometrical patterns on friction can be applied to various tribological systems; earthquake dynamics [143] and anisotropic friction by surface patterns [171, 172] have been modelled based on their macroscopic surface geometry. A similar model has been introduced to describe the microscopic friction coefficient based on the surface height variations of surfaces [173, 174]. However, modelling the influence of the surface roughness with this geometrical model was not satisfactory; the real contact area that is formed and the shear stress prior to sliding on the asperity-level is rather more complex [114]. In the model presented here, we separate the rather complex (adhesive) friction coefficient μ_0 from the geometrical part for macroscopic surface roughness.

In summary, with artificial macroscopic surface roughness the sliding friction can be tuned by more than an order of magnitude which can be explained using a simple geometrical model that takes into account the interlocking between the two surfaces. The slope, quantified with the angle, of the surface patterning and the commensurability of patterned surfaces enables direct control on the sliding friction. In addition, a Kirigami metamaterial surface allows to apply this understanding of geometrical friction to enable external and on-demand control of the friction force.